Zhang *et al.*
EURASIP Journal on Advances in Signal Processing (2022) 2022:66
https://doi.org/10.1186/s13634-022-00896-x

EURASIP Journal on Advances in Signal Processing

RESEARCH Open Access

Three-dimensional SAR imaging with sparse linear array using tensor completion in embedded space

Siqian Zhang[1*], Ding Ding[2], Chenxi Zhao[1] and Lingjun Zhao[1]

*Correspondence:
zhangsiqian@nudt.edu.cn

[1] State Key Laboratory of Complex Electromagnetic Environment Effects on Electronics and Information System, College of Electronic Science, National University of Defense Technology, Changsha 410073, China
[2] Center for Teaching and Research Service, National University of Defense Technology, Changsha 410073, China

Abstract

Due to the huge data storage and transmission pressure, sparse data collection strategy has provided opportunities and challenges for 3D SAR imaging. However, sparse data brought by the sparse linear array will produce high-level side-lobes, as well as the aliasing and the false-alarm targets. Simultaneously, the vectorizing or matrixing of 3D data makes high computational complexity and huge memory usage, which is not practicable in real applications. To deal with these problems, tensor completion (TC), as a convex optimization problem, is used to solve the 3D sparse imaging problem efficiently. Unfortunately, the traditional TC methods are invalid to the incomplete tensor data with missing slices brought by sparse linear arrays. In this paper, a novel 3D imaging algorithm using TC in embedded space is proposed to produce 3D images with efficient side-lobes suppression. With the help of sparsity and low-rank property hidden in the 3D radar signal, the incomplete tensor data is taken as the input and converted into a higher order incomplete Hankel tensor by multiway delay embedding transform (MDT). Then, the tucker decomposition with incremental rank has been applied for completion. Subsequently, any traditional 3D imaging methods can be employed to obtain excellent imaging performance for the completed tensor. The proposed method achieves high resolution and low-level side-lobes compared with the traditional TC-based methods. It is verified by several numerical simulations and multiple comparative studies on real data. Results clearly demonstrate that the proposed method can generate 3D images with small reconstruction error even when the sparse sampling rate or signal to noise ratio is low, which confirms the validity and advantage of the proposed method.

Keywords: 3D SAR, Incomplete data, Low rank, Tensor completion, Signal reconstruction

1 Introduction

On the basis of traditional two-dimensional SAR, three-dimensional synthetic aperture radar (3D SAR) system can obtain the height information of a target or scene and construct a 3D imagery with a high resolution, which has an important significance for military and civilian practical applications. In these years, a number of 3D SAR imaging technologies have arisen, such as Interferometric SAR (InSAR) [1, 2], Tomographic SAR

[3], Circular SAR (CSAR) [4–6] and Linear Array SAR (LASAR) [7–9]. The former two types of SAR systems are based on the interferometric technique, in which multiple antennas are used to observe the target from different angles and obtain the 3D elevation information [1]. However, these methods do not result in a real 3D imagery [1–3]. CSAR achieves 3D imaging capability by controlling the circular trajectory of the flight, which requires precise control of the flight trajectory [10]. In view of the above problems, Gierull introduced the concept of downward-looking line array (DLLA) SAR [11]. DLLA 3D SAR [12–14] synthesizes virtual 2-D aperture by real and synthetic aperture, and achieves accurate height-oriented imaging by pulse compression. The downward looking mode can effectively solve the issues of shadowing and overlaying caused by the traditional side looking.

Moreover, the disadvantages of massive data storage and transmission burden make the LASAR system meet many difficulties in the practical application as it requires densely sampled data in three dimensions. As a result, sparse data collection strategy can greatly reduce the data collection burden, which creates powerful incentives to research 3D SAR sparse imaging. Unfortunately, when the conventional imaging algorithms meet sparsely collected data, the quality of 3D images deteriorates dramatically with unpredictable sidelobe and false targets behavior. The targets cannot be exactly focused because the signal sampling no longer meets the Nyquist sampling rate.

The methods for reconstructing sparse signal can be grouped into two categories. The first category is to recover sparse signals with overwhelming probability directly through a finite number of measurements based on compressive sensing (CS) theory [15–17]. However, high accuracy of the measurement matrix is required to ensure the quality of the 3D images. In comparison, the methods belonging to the second category complete the lost samples of a sparse signal using only its available elements. The key is to establish the relationship between existing entries and the missing ones [18]. As a representative technique, tensor completion constructs the potential connections between the existing and the missing elements by leveraging the low-rankness [19]. Meanwhile, the intrinsic structure of the high-dimensional data will not be destroyed by tensor [18] because of no dimensionality reduction. Therefore, the lost elements in sparse signal can be recovered by solving a convex optimization problem when the echo data tensor meets the low-rankness [20]. Some heuristic algorithms [18, 21–24] were proposed to estimate the lost values iteratively and have been proven to be effective in 3D SAR sparse imaging applications [12, 25, 26]. However, in fact the echoed data acquired by the sparse linear array can be viewed as a 3-order incomplete tensor with randomly missing slices. In this case, the tensor completion methods mentioned above generally failure recover the missing data element, which causes the unacceptable imaging performance. Fortunately, by applying multi-dimensional Hankelization to the incomplete data, a good idea of data completion has been proposed [27, 28].

A novel imaging algorithm using TC in embedded space is proposed in this manuscript for sparse array 3D SAR. Firstly, the signal model of the 3D sparse array SAR is modeled in tensor space. By using tensor, it is possible to mine the internal properties hidden in the 3D data. Secondly, the inadequate data with missing slices is represented as a Hankel tensor with higher order by MDT. Due to the Hankel structure, this tensor with higher order is expected to have a relatively low rank. The lost elements are then completed

perfectly by a tucker decomposition in the embedded space and subsequently the 3D imagery can be focused by the various 3D imaging approaches. Finally, the effectiveness and the accuracy of the proposed algorithm have been evaluated by various experiment results of simulated and measured data.

The paper sections are shown below. Section 2 briefly introduces the notations and formulas of tensor as the preliminaries and backgrounds. In Sect. 3, the construction of 3D sparse array SAR signal model in the tensor space is given. In Sect. 4, we discuss the low rank and sparse property and then present a 3D imaging algorithm using TC in embedded space for 3D sparse array SAR. Section 5 shows experimental findings that demonstrate the validity of the presented method. Finally, conclusions are drawn in Sect. 6.

2 Notation and preliminaries

This section first introduces the notations and formulas related to tensor or tensor operation as a preparation for the following algorithm derivation, as shown in Table 1.

3 Signal model

Figure 1 illustrates the imaging geometric relationship of 3D sparse array SAR. Suppose that the aircraft flies at the altitude H with a speed V_a. Under the wings of the aircraft, a number of antenna arrays suspended at unequal intervals made up a sparse linear array with the length of L_y. In the 3D space coordinate system, three orthogonal axes represent the azimuth, cross-tack and altitude, corresponding to the aircraft flight direction, linear array direction and radar irradiation direction, respectively.

Table 1 Notations and preliminaries

Definitions	Notations and formulas	Notes
Vector	$\mathbf{b}$	
Matrix	$\mathbf{B}$	
Tensor	$\boldsymbol{\mathcal{A}}$	$\boldsymbol{\mathcal{A}}^{(i)}$—the ith matrix in a sequence
Unfolding/matricization	The i-mode unfolding/matricization: $\boldsymbol{\mathcal{A}}_{(i)}$	Unfolding a tensor to a matrix
Frobenius norm	$\|\boldsymbol{\mathcal{A}}\|_F = \sqrt{\sum_{m_1}\sum_{m_2}\cdots\sum_{m_l} a^2_{m_1 m_2 \cdots m_l}}$	$\boldsymbol{\mathcal{A}} \in \mathbb{C}^{M_1 \times M_2 \times \cdots \times M_l}$
Tensor multiplication	The i-mode product of tensor $\boldsymbol{\mathcal{A}}$ and matrix $\mathbf{B}$: $(\boldsymbol{\mathcal{A}} \times_i \mathbf{B})_{m_1 \cdots m_{i-1} k m_{i+1} \cdots m_l} = \sum_{m_i=1}^{M_i} a_{m_1 m_2 \cdots m_l} b_{k m_i}$	
Tucker decomposition	$\boldsymbol{\mathcal{A}} = \boldsymbol{\mathcal{C}} \times_1 \mathbf{F}^{(1)} \times_2 \mathbf{F}^{(2)} \cdots \times_l \mathbf{F}^{(l)}$	$\boldsymbol{\mathcal{C}}$ is core tensor $\mathbf{F}^{(i)}$ is factor matrix
Multi-linear tensor product	Multi-linear tensor product: $\boldsymbol{\mathcal{C}} \times \{\mathbf{F}\} = \boldsymbol{\mathcal{C}} \times_1 \mathbf{F}^{(1)} \times_2 \mathbf{F}^{(2)} \cdots \times_l \mathbf{F}^{(l)}$ Multi-linear tensor product with the i-th mode excluded: $\boldsymbol{\mathcal{C}} \times_{-i} \{\mathbf{F}\} = \boldsymbol{\mathcal{C}} \times_1 \mathbf{F}^{(1)} \cdots \times_{i-1} \mathbf{F}^{(i-1)} \times_{i+1} \mathbf{F}^{(i+1)} \cdots \times_l \mathbf{F}^{(l)}$	$\{\mathbf{F}\} = \{\mathbf{F}^{(i)}\}_{i=1}^{l}$ is a set of the factor matrices
Rank-one tensor	If $\boldsymbol{\mathcal{A}}$ can be expressed as an outer product of vectors, i.e., $\boldsymbol{\mathcal{A}} = \mathbf{x}^{(1)} \circ \mathbf{x}^{(2)} \circ \cdots \circ \mathbf{x}^{(l)}$, it satisfies rank-one tensor	$\circ$ denotes the outer product of vectors
Tensor rank	rank($\boldsymbol{\mathcal{A}}$)	The minimum quantity of rank-one tensors which make up $\boldsymbol{\mathcal{A}}$ by their sum

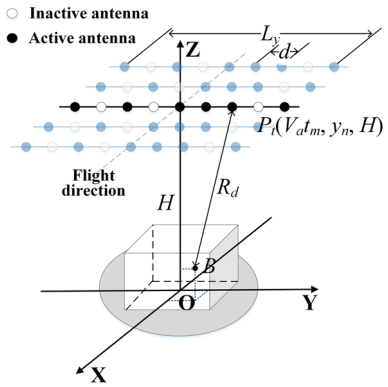

Fig. 1 Imaging geometric relationship of 3D sparse array SAR

From the theory of scattering center model [29], the large volume target consists of a finite number of scattering points. The activate antennas transmit a step frequency signal. This modulated signal consists of a set of K pulses with a reference frequency f_0. The step frequency increases sequentially in a constant frequency increment Δf. The signal reaches target B and then is reflected back to be received by the activate antennas. After a double-way propagation distance, the receiving antenna can obtain the echo signal E as

$$E = A\gamma \exp\left[-2\pi j(f_0 + k\Delta f)(\tau - 2R_d/c)\right] \tag{1}$$

where A is the amplitude. γ denotes the backscattering coefficient of the target. τ is the time variable. The one-way distance of signal propagation R_d is indicated as the distance between the transmitting/receiving antenna $P_t = (V_a t_m, y_n, H)$ and the target $P_B = (x_B, y_B, z_B)$.

$$\begin{aligned} R_d &= \sqrt{(V_a t_m - x_B)^2 + (y_n - y_B)^2 + (H - z_B)^2} \\ &= \sqrt{R_0^2 - 2(V_a t_m x_B + y_n y_B + H z_B) + x_B^2 + y_B^2 + z_B^2} \\ &\approx R_0 \left[1 - \frac{2(V_a t_m x_B + y_n y_B + H z_B)}{2R_0^2} + \frac{x_B^2 + y_B^2 + z_B^2}{2R_0^2}\right] \\ &\approx R_0 - \left(\frac{V_a t_m x_B}{R_0} + \frac{y_n y_B}{R_0} + \frac{H z_B}{R_0}\right) \end{aligned} \tag{2}$$

where $R_0 = \sqrt{(V_a t_m)^2 + y_n^2 + H^2}$ indicates Zero-Doppler distance. The first approximately equal sign is established according to Fresnel approximation. It can be seen that the third part can be neglected due to the far-field condition, i.e., $R_0 \gg x_B, y_B, z_B$.

Since the sample on a 3D signal grid is discrete, the received data by these scatterers can be expressed as

$$E = \sum_m \sum_n \sum_k \gamma(x_B, y_B, z_B) \exp\left(-4\pi j \frac{R_0}{\lambda}\right) \tag{3}$$

Further simplification, the part of constant $\exp(-4\pi jR_0/\lambda)$ is ignorable in the below content. Let three variables δ_x, δ_y, δ_z are introduced as

$$\delta_x = \frac{2V_a t_m}{\lambda R_0}, \quad \delta_y = \frac{2y_n}{\lambda R_0}, \quad \delta_z = \frac{2H}{\lambda R_0} \tag{4}$$

Therefore, the echo signal can be represented as follow format. It can be view as a generic signal model for 3D SAR imaging.

$$E(\delta_x, \delta_y, \delta_z) = \sum_m \sum_n \sum_k \gamma(x_B, y_B, z_B) \exp\left[2\pi j(\delta_x x_B + \delta_y y_B + \delta_z z_B)\right] \tag{5}$$

In order to obtain the 3D imagery in tensor space, the above signal model can be represented into tensor form. The imaging scene can be divided into grids at equal intervals with the size of $P \times Q \times L$. That is to say, if there is a scattering point in the grid, γ is not equal to 0. Thus, Eq. (5) can be re-described as

$$E(m, n, k) = \sum_p \sum_q \sum_l \gamma(p, q, l) \exp\left[2\pi j(\delta_x x_p + \delta_y y_q + \delta_z z_l)\right] \tag{6}$$

The tensor representation of the signal model can be described as

$$\boldsymbol{\mathcal{E}} = \boldsymbol{\mathcal{G}} \times_1 \boldsymbol{\Phi}_x \times_2 \boldsymbol{\Phi}_y \times_3 \boldsymbol{\Phi}_z \tag{7}$$

where $\boldsymbol{\mathcal{E}}$ is tensor format of the echo E with the order of $M \times N \times K$, $\boldsymbol{\mathcal{G}}$ is tensor format of the backscattering coefficient γ with the order of $P \times Q \times L$, $\times_i, i = 1, 2, 3$ represents tensor multiplication. $\boldsymbol{\Phi}_x$ is the azimuth steering vector matrix, $\boldsymbol{\Phi}_y$ is the cross-track steering vector matrix, $\boldsymbol{\Phi}_z$ is the range steering vector matrix.

$$\begin{aligned} \boldsymbol{\Phi}_x &= \exp(2\pi j \delta_x x_p) \in \mathbb{C}^{M \times P} \\ \boldsymbol{\Phi}_y &= \exp(2\pi j \delta_y y_q) \in \mathbb{C}^{N \times Q} \\ \boldsymbol{\Phi}_z &= \exp(2\pi j \delta_z z_l) \in \mathbb{C}^{K \times L} \end{aligned} \tag{8}$$

4 Methods

Before reconstruction the target, we consider recovering the lost data elements first. Then, a traditional 3D imaging algorithm is exploited to obtain a more excellence 3D imagery. However, the echo data acquired by the sparse linear array can be viewed as a 3-order incomplete tensor with randomly missing slices. In this case, it is difficult for the traditional TC approach to recover the lost data elements, which cause the unacceptable imaging performance.

In this section, we present a novel 3D imaging algorithm for sparse array SAR using TC in embedded space to solve the above problem. Figure 2 depicts the flow diagram of this 3D sparse array SAR imaging method based on the echo tensor with missing slices. The algorithm includes two parts: tensor completion and 3D imaging, where the part of tensor completion contains MDT, low-rank tensor approximation, and inverse MDT steps.

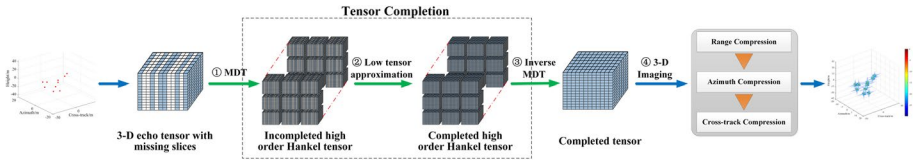

Fig. 2 The flow diagram of the proposed method

4.1 Property analysis for signal tensor

First, we discuss the sparse property based on the signal model in (6), which helps to perform 3D image reconstruction from a sparse signal tensor. For 3D sparse array SAR, massive quantity of non-target areas exists in the 3D scene. That means the sum of the backscattered responses of few prominent scatters constitutes the 3D radar image $\mathcal{G}$, which means that $\mathcal{G}$ is expected to be sparse.

Then, the prerequisite of tensor completion is the low-rank property. The signal data for one scattering point B is constructed as

$$E(m,n,k) = \gamma_B \exp\left[2\pi j(\delta_x x_B + \delta_y y_B + \delta_z z_B)\right] \tag{9}$$

Thus, the tensor representation of signal $\mathcal{E}$ is expressed as

$$\mathcal{E} = \gamma \mathbf{\Phi}_x(:,x) \circ \mathbf{\Phi}_y(:,y) \circ \mathbf{\Phi}_z(:,z) \tag{10}$$

The operator of outer product indicates as $\circ$. Since $\mathcal{E}$ is expressed as an outer product of vectors, it satisfies a rank-one tensor. It also shows that $\mathcal{E}$ is a low-rank tensor.

Due to the superposition of signals from several scatterers, the final signal $\mathcal{E}$ can be characterized as a linear combination of the corresponding 3-mode rank-one tensor.

$$\mathcal{E} = \sum_{b=1}^{B} \gamma_b \mathbf{\Phi}_x(:,x_b) \circ \mathbf{\Phi}_y(:,y_b) \circ \mathbf{\Phi}_z(:,z_b) \tag{11}$$

The minimum quantity of rank-one tensors which make up $\mathcal{E}$ by their sum (see Sect. 2) denotes the rank of $\mathcal{E}$. That means the rank of tensor $\mathcal{E}$ cannot exceed B. In addition, a few number of strong scattering points form the image scene, thus $B \ll PQL$, and further derived that $\text{rank}(\mathcal{E}) \leq B \ll PQL$. Hence, if the target is sparse, then the tensor $\mathcal{E}$ has the property of low CP-rank.

4.2 MDT and inverse MDT

Given that the 3-order echo tensor $\mathcal{E}$ is transformed by a delay embedding with parameters $\boldsymbol{\xi} = \{\xi_1, \xi_2, \xi_3\} \in \mathbb{N}^3$ and $\mathbf{\Psi} = \{M, N, K\}$. This processing includes two steps: duplication step and folding step [28], as shown in Fig. 3.

First, the MDT produces the low order tensor $\mathcal{E}$ into a duplicated high order tensor, which is called as "Hankelization" [30]. Consider the duplication matrices are satisfied as

$$\begin{aligned} \mathbf{D}_1 &\in \{0,1\}^{\xi_1(M-\xi_1+1)\times M} \\ \mathbf{D}_2 &\in \{0,1\}^{\xi_2(N-\xi_2+1)\times N} \\ \mathbf{D}_3 &\in \{0,1\}^{\xi_3(K-\xi_3+1)\times K} \end{aligned} \tag{12}$$

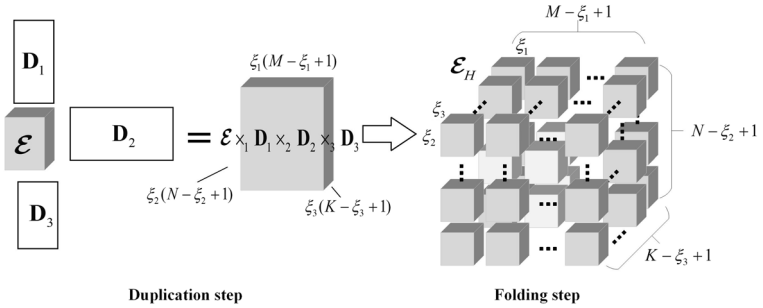

Fig. 3 MDT processing for a tensor

Then the MDT can be obtained by

$$\mathcal{H}_{\boldsymbol{\xi}}(\boldsymbol{\mathcal{E}}) = \text{fold}_{(\boldsymbol{\psi},\boldsymbol{\xi})}(\boldsymbol{\mathcal{E}} \times_1 \mathbf{D}_1 \times_2 \mathbf{D}_2 \times_3 \mathbf{D}_3) \tag{13}$$

where $\text{fold}_{(\boldsymbol{\psi},\boldsymbol{\xi})} = \text{unfold}^{-1}_{(\boldsymbol{\psi},\boldsymbol{\xi})}$ denotes a folding operator from a low order tensor to a high order one. Here a 6-th order tensor with $\xi_1 \times (M - \xi_1 + 1) \times \xi_2 \times (N - \xi_2 + 1) \times \xi_3 \times (K - \xi_3 + 1)$ is constructed from the input 3-th order tensor with $\xi_1(M - \xi_1 + 1) \times \xi_2(N - \xi_2 + 1) \times \xi_3(K - \xi_3 + 1)$.

In contrast, the inverse MDT transform can be decomposed into two steps: a matricization operation (also known as unfolding) and the Moore–Penrose pseudo-inverse $\mathbf{D}^{\dagger} = (\mathbf{D}^T\mathbf{D})^{-1}\mathbf{D}^T$. Thus, the Hankel tensor $\boldsymbol{\mathcal{E}}_H$ after the inverse MDT processing is presented as

$$\mathcal{H}^{-1}_{\boldsymbol{\xi}}(\boldsymbol{\mathcal{E}}_H) = \text{unfold}_{(\boldsymbol{\psi},\boldsymbol{\xi})}(\boldsymbol{\mathcal{E}}_H) \times_1 \mathbf{D}_1^{\dagger} \times_2 \mathbf{D}_2^{\dagger} \times_3 \mathbf{D}_3^{\dagger} \tag{14}$$

4.3 Low-rank tensor approximation

According to (13), the incomplete tensor $\boldsymbol{\mathcal{E}} \in \mathbb{C}^{M\times N\times K}$ and its mask tensor $\boldsymbol{\mathcal{M}} \in \{0,1\}^{M\times N\times K}$ can be transformed by MDT, which are given by

$$\begin{aligned} \boldsymbol{\mathcal{E}}_H &= \mathcal{H}(\boldsymbol{\mathcal{E}}) \in \mathbb{C}^{J_1\times\cdots\times J_I} \\ \boldsymbol{\mathcal{M}}_H &= \mathcal{H}(\boldsymbol{\mathcal{M}}) \in \{0,1\}^{J_1\times\cdots\times J_I} \end{aligned} \tag{15}$$

where $I = 6$ because the Hankel tensor $\boldsymbol{\mathcal{E}}_H$ is a 6-th order tensor here. The zero elements in $\boldsymbol{\mathcal{M}}_H$ correspond to the lost entry; otherwise, the one element corresponds to the available entry.

Here, we can solve the low-rank tensor approximation by tucker decomposition. Hence, the solution of the optimization problem can be converted into the following form.

$$\min_{\boldsymbol{\mathcal{C}},\{\mathbf{F}^{(i)}\}_{i=1}^{I}} \|\boldsymbol{\mathcal{M}}_H \circledast (\boldsymbol{\mathcal{E}}_H - \boldsymbol{\mathcal{C}} \times \{\mathbf{F}\})\|_F^2, \quad \text{s.t.} \quad \boldsymbol{\mathcal{C}} \in \mathbb{R}^{R_1\times\cdots\times R_I}, \ \mathbf{F}^{(i)} \in \mathbb{R}^{J_i\times R_i}(\forall i) \tag{16}$$

where $\circledast$ denotes the element wise Hadamard product.

The above equation is not a convex issue and the solution is not unique [20]. For the tensor with the complete elements, its stationary point can be efficiently obtained by

the alternating least squares (ALS) [20] for tucker decomposition, whereas for the tensor with lost elements, we can address this optimization problem effectively by gradient descent method [31] and manifold optimization [32]. It is obvious that the step-size parameter affects the efficiency of both algorithms. Therefore, an auxiliary function [28] is introduced as

$$f(\alpha|\alpha') := \|\boldsymbol{\mathcal{M}}_H \circledast (\boldsymbol{\mathcal{E}}_H - \boldsymbol{\mathcal{T}}_\alpha)\|_F^2 + \left\|\overline{\boldsymbol{\mathcal{M}}}_H \circledast (\boldsymbol{\mathcal{T}}_{\alpha'} - \boldsymbol{\mathcal{T}}_\alpha)\right\|_F^2 \tag{17}$$

where a parameter set $\alpha = \{\mathcal{C}, \mathbf{F}^{(1)}, \mathbf{F}^{(2)} \ldots, \mathbf{F}^{(I)}\}$, $\boldsymbol{\mathcal{T}}_\alpha = \mathcal{C} \times \{\mathbf{F}\}$ denotes a tucker decomposition, and $\overline{\boldsymbol{\mathcal{M}}}_H$ as a complement set of $\boldsymbol{\mathcal{M}}_H$ is equal to $1 - \boldsymbol{\mathcal{M}}_H$.

According to [28], we can transform the auxiliary function into

$$\begin{aligned} f(\alpha|\alpha') &= \|\boldsymbol{\mathcal{M}}_H \circledast (\boldsymbol{\mathcal{E}}_H - \boldsymbol{\mathcal{T}}_\alpha)\|_F^2 + \left\|\overline{\boldsymbol{\mathcal{M}}}_H \circledast (\boldsymbol{\mathcal{T}}_{\alpha'} - \boldsymbol{\mathcal{T}}_\alpha)\right\|_F^2 \\ &= \left\|(\boldsymbol{\mathcal{M}}_H \circledast \boldsymbol{\mathcal{E}}_H + \overline{\boldsymbol{\mathcal{M}}}_H \circledast \boldsymbol{\mathcal{T}}_{\alpha'}) - (\boldsymbol{\mathcal{M}}_H + \overline{\boldsymbol{\mathcal{M}}}_H) \circledast \boldsymbol{\mathcal{T}}_\alpha\right\|_F^2 \\ &= \|\boldsymbol{\mathcal{X}} - \boldsymbol{\mathcal{T}}_\alpha\|_F^2 \end{aligned} \tag{18}$$

Clearly, there is a two-step processing composing the auxiliary function minimization solution. First, the auxiliary tensor $\boldsymbol{\mathcal{X}}$ can be calculated by

$$\boldsymbol{\mathcal{X}} = \boldsymbol{\mathcal{M}}_H \circledast \boldsymbol{\mathcal{E}}_H + \overline{\boldsymbol{\mathcal{M}}}_H \circledast \boldsymbol{\mathcal{T}}_{\alpha'} \tag{19}$$

Then, the factor matrices $\{\mathbf{F}\}$ and the core tensor $\mathcal{C}$ are updated by using the ALS to optimize

$$\min_{\mathcal{C}, \{\mathbf{F}^{(i)}\}_{i=1}^I} \|\boldsymbol{\mathcal{X}} - \mathcal{C} \times \{\mathbf{F}\}\|_F^2, \quad \text{s.t. } \mathbf{F}^{(i)T}\mathbf{F}^{(i)} = \mathbf{I}_{R_i} (\forall i) \tag{20}$$

In order to the non-uniqueness of the tensor $\boldsymbol{\mathcal{T}}$ solution, the rank increment strategy is integrated into tucker-based completion, which has been discussed in [28]. Specifically, a very low-rank tucker decomposition is first set up and used as initialization to obtain a higher-rank decomposition. Following that the rank is updated iteratively until the noise condition is less than a threshold. In short, the algorithm of low-rank tensor approximation can be summarized step by step as follows.

1: Set a low rank sequence $R_i = 1$ where $i = 1, \ldots, 6$ as the initial value.

2: According to Eqs. (19) and (20), compute $\mathcal{C}$ and $\{\mathbf{F}^{(i)}\}_{i=1}^I$ with the initial rank sequence R_i. $\boldsymbol{\mathcal{T}} = \mathcal{C} \times \{\mathbf{F}\}$ is calculated accordingly.

3: Judge whether $\|\boldsymbol{\mathcal{M}}_H \circledast (\boldsymbol{\mathcal{E}}_H - \boldsymbol{\mathcal{T}})\|_F^2$ as a noise condition is not larger than a noise threshold parameter η. If it is satisfied, the algorithm is terminated; otherwise, the algorithm continues to execute.

4: update the parameter $i' = \text{argmax}_i \left\|(\boldsymbol{\mathcal{M}}_H \circledast (\boldsymbol{\mathcal{E}}_H - \boldsymbol{\mathcal{T}})) \times_{-i} \{\mathbf{F}^T\}\right\|_F^2$ and increment $R_{i'}$, and then go back to step 2.

4.4 3D image reconstruction

After the completely sampled 3D data has been recovered by TC mentioned above, 3D imagery can be focused exactly by the Fourier transform-based technologies. Further, some super-resolution imaging algorithms such as the spectrum estimation strategies [33] also can be employed.

To summarize, the proposed method for 3D sparse array SAR imaging using TC in embedded space is shown in Algorithm 1. It is clear that the sparse tensor is transformed to an incomplete high order Hankel tensor by MDT first. Next, low-rank tensor approximation is leveraged to complete the higher order tensor and in the next step converted to the full-sampled data tensor by inverse MDT. Last, the 3D imagery can be focused by applying the 3D Range Doppler (RD) algorithm. More details of 3D RD algorithm can be found in [34].

Algorithm 1 3D SAR sparse imaging using tensor completion in embedded space

Input: sparse data tensor $\mathcal{E} \in \mathbb{C}^{M\times N\times K}$, a duplication matrix $\mathbf{D}_1$, $\mathbf{D}_2$ and $\mathbf{D}_3$, mask tensor $\mathcal{M} \in \{0,1\}^{M\ N\times K}$, the rank sequence $\{\mathbf{L}_1,\mathbf{L}_2,\cdots,\mathbf{L}_6\}$, parameter ξ, η and tol.

Output: 3D image $\mathcal{I}$

Initialization: $k_i \leftarrow 1$, $R_i \leftarrow \mathbf{L}_i(k_i)(\forall i)$, $\mathcal{C} \in \mathbb{C}^{R_1\times R_2\times\cdots\times R_6}$, and $\{\mathbf{F}^{(i)}\}_{i=1}^{6}$

// **Step 1: MDT**

(1) duplicate tensor $\mathcal{E} \leftarrow \mathcal{E}\times_1 \mathbf{D}_1 \times_2 \mathbf{D}_2 \times_3 \mathbf{D}_3$

(2) folding operation $\mathcal{E}_H \leftarrow \text{fold}_{(\Psi,\xi)}(\mathcal{E})$

// **Step 2: Tensor approximation**

(3) $\mathcal{T} \leftarrow \mathcal{C}\times\{\mathbf{F}\}$

(4) $f_1 \leftarrow \left\|\mathcal{M}_H \circledast \left(\mathcal{E}_H - \mathcal{T}\right)\right\|_F^2$

(5) **repeat**

(6) $\mathcal{X} = \mathcal{M}_H \circledast \mathcal{E}_H + \overline{\mathcal{M}}_H \circledast \mathcal{T}$

(7) **for** i = 1 to 6 **do**

(8) $\mathcal{E}_H \leftarrow \mathcal{X}\times_{-i}\{\mathbf{F}^T\}$

(9) $\mathbf{F}^{(i)} \leftarrow R_i$

(10) **end for**

(11) $\mathcal{C} \leftarrow \mathcal{X}\times\{\mathbf{F}^T\}$

(12) $\mathcal{T} \leftarrow \mathcal{C}\times\{\mathbf{F}\}$

(13) $f_2 \leftarrow \left\|\mathcal{M}_H \circledast \left(\mathcal{E}_H - \mathcal{T}\right)\right\|_F^2$

(14) **if** $|f_2 - f_1| \le tol$ **then**

(15) $\tilde{\mathcal{T}} \leftarrow \mathcal{M}_H \circledast (\mathcal{E}_H - \mathcal{T})$

(16) $i' \leftarrow \arg\max_i \left\|\tilde{\mathcal{T}}\times_{-i}\{\mathbf{F}^T\}\right\|_F^2$

(17) $k_{i'} \leftarrow k_{i'} + 1$, and $R_{i'} \leftarrow \mathbf{L}_{i'}(k_{i'})$

(18) **else**

(19) $f_1 \leftarrow f_2$

(20) **end if**

(21) **until** $f_2 \le \eta$

(22) $\mathcal{T} \leftarrow \mathcal{C}\times\{\mathbf{F}\}$

// **Step 3: IMDT**

(23) Moore-Penrose pseudo-inverse $\mathbf{D}^{\dagger} \leftarrow (\mathbf{D}^T\mathbf{D})^{-1}\mathbf{D}^T$

(24) vectorization operation $\mathcal{H}_{\xi}^{-1}(\mathcal{T}) = \text{unfold}_{(\psi,\xi)}(\mathcal{T})\times_1 \mathbf{D}_1^{\dagger} \times_2 \mathbf{D}_2^{\dagger} \times_3 \mathbf{D}_3^{\dagger}$

(25) obtain the completed tensor $\mathcal{T} \leftarrow \mathcal{H}_{\xi}^{-1}\left(\mathcal{T}\right)$.

// **Step 4: 3D Image Reconstruction**

(26) $\mathcal{I} = \text{3D-RD}(\mathcal{T})$, where 3D-RD represents 3D RD algorithm.

Table 2 Running environment of our experiments

Software	Processor	Memory	Operating system
MATLAB R2019a	Intel Core i9-9900KF, 3.60 GHz	128G	Microsoft Windows 7

Table 3 System parameters used in the simulations

Parameter	Value
Reference frequency (f_0)	10 GHz
Frequency step (Δf)	100 MHz
Signal bandwidth (B_r)	150 MHz
Fly elevation (H)	1000 m
Fly speed (V_a)	200 m/s
Pulse repeat frequency (PRF)	1000 Hz
Number of range samples (K)	120
Number of azimuth samples (M)	200
Length of linear array (L_y)	6 m

5 Results and discussion

In this section, the validity and accuracy of the proposed 3D imaging algorithm is evaluated by the simulated and real datasets. The running environment carried out in our experiments is listed in Table 2.

5.1 Verification of the proposed algorithm using simulated dataset

First, the simulations of the imaging distributed scene for 3D sparse array SAR are presented to verify the validity of the proposed algorithm. An X-band SAR and a single scatterer located at (3 m, 0 m, − 1 m) are utilized. Table 3 lists the parameters used in the simulations. A full-sample 3D data in this simulation is collected by a uniform virtual linear array. The virtual array of 120 elements is built by using 4 transmit and 30 receive elements with MIMO technique. SNR = 10 dB. The first line in Fig. 4 shows the 3D imaging results by using 3D RD method with full-sampled data.

The sparse sampling rate (SSR) is denoted by the number ratio of the observed samples to the all samples. Here, we use a sparse linear array by randomly selecting 60 elements to produce the sparse data, i.e., SSR = 50%. This sparse data can be seen as a 3D tensor data with the missing slice. We pad the lost samples with zeros and then apply the different imaging algorithms to acquire 3D images. Figure 4 shows the 3D imaging results with different methods. Images are obtained by the conventional 3D RD method and the proposed method in the second and third line, respectively. The proposed method can recover the missing slices exactly. We set $\boldsymbol{\xi} = (32, 1, 1)$ and a (120, 200, 120) echo data was converted into a (32, 89, 1, 200, 1, 120) tensor. This Hankel tensor was re-expressed as a fourth-order tensor with (32, 89, 120, 200). Thus, we set the rank sequences as $\mathbf{L}_1 = [1\ 2\ 4\ 8\ 16\ 32]$, $\mathbf{L}_2 = [1\ 2\ 4\ 8\ 16\ 32\ 64\ 84]$, $\mathbf{L}_3 = [1\ 2\ 4\ 8\ 16\ 32\ 64\ 96\ 118]$, and $\mathbf{L}_4 = [1\ 2\ 4\ 8\ 16\ 32\ 64\ 96\ 128\ 160\ 192]$.

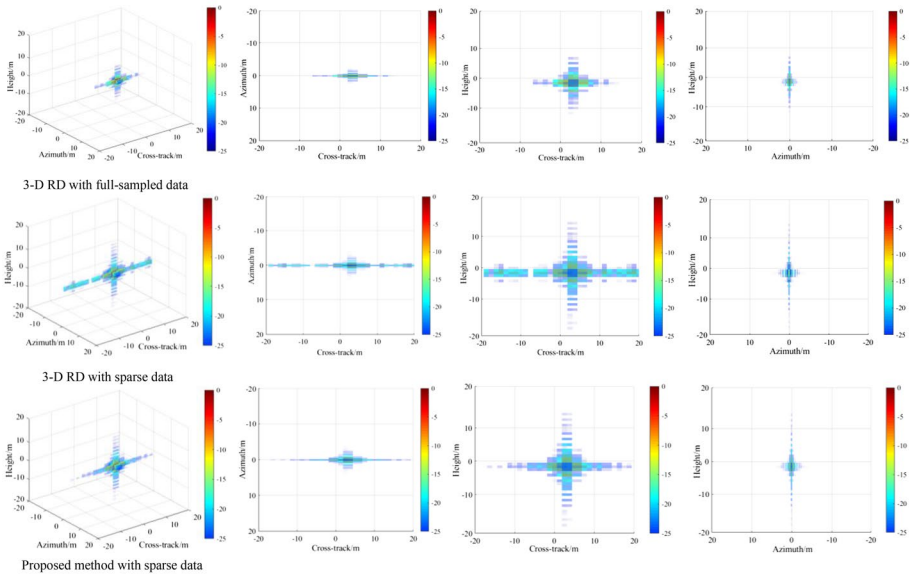

(a) 3-D imaging result (b) Cross-track-azimuth slice (c) Cross-tack-height slice (d) Azimuth-height slice

Fig. 4 3D imaging results of 3D RD and proposed method with 100% data or 50% sparse data. The SNR is set as 10 dB. The limited amplitude is − 25 dB

Table 4 Evaluated indexes with different methods

(*X*, *Y*, *Z*)	RD (100% data)	RD (50% sparse data)	Proposed method (50% sparse data)
PSLR (dB)	(− 6.3010, − 13.9317, − 9.0579)	(− 5.7059, − 13.8840, − 8.5366)	(− **6.3652**, − **13.9663**, − **9.1599**)
ISLR (dB)	(− 6.2692, − 4.1744, − 2.7365)	(− 1.9645, − 3.9009, − 2.5161)	(− **6.3401**, − **4.2311**, − **2.7787**)

The optimal values are shown in bold

From Fig. 4, the scatterer is recovered with high-level side-lobes along the cross-track direction by the 3D RD algorithm. For comparison, the proposed method can focus the scatterer precisely because of TC processing with MDT. Noted that there is no significant change along both azimuth and height directions because the missing slice is only appeared along the cross-tack direction. The peak sidelobe ratio (PSLR) and integrated sidelobe ratio (ISLR) as evaluated indexes are leveraged, which are shown in Table 4 for the point target. Here the best values are emphasized in bold font. As we can see from the cross-track direction, PSLR and ISLR values of 3D RD with sparse data deteriorate significantly, whereas the proposed method obtains the best performances, which is much closer to the corresponding indexes with 100% data. Moreover, PSLR and ISLR values in the other two directions obtain the similar results among these algorithms.

5.2 Performance comparison with different algorithms

Furthermore, the performance of the proposed method is compared with those of other different algorithms including the conventional TC algorithms: high accuracy low rank tensor completion (HaLRTC) and tucker decomposition (TDC). Consider a target

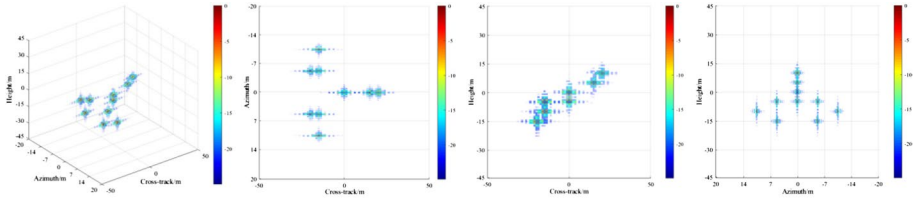

(a) 3-D imaging result (b) Cross-track-azimuth slice (c) Cross-tack-height slice (d) Azimuth-height slice

Fig. 5 3D imaging results of 3D RD with 100% data. The SNR is set as 10 dB. The limited amplitude is — 25 dB

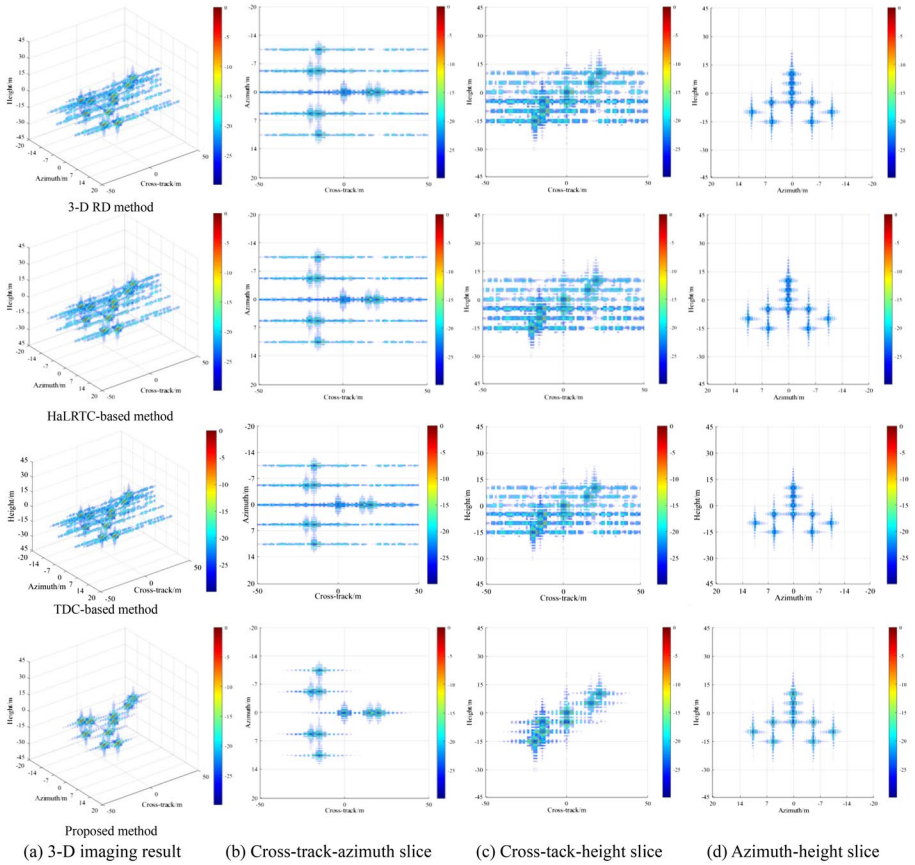

(a) 3-D imaging result (b) Cross-track-azimuth slice (c) Cross-tack-height slice (d) Azimuth-height slice

Fig. 6 3D imaging results of various methods with 80% sparse data. The SNR is set as 10 dB. The limited amplitude is — 25 dB

consisting of 10 scattering points with the same amplitude. 3D RD method is chosen as a baseline method for comparison and the imaging results are illustrated in Fig. 5 with full-sampled data.

Figure 6 illustrates the results obtained by various methods. From top to bottom, images are acquired by the 3D RD method, the HaLRTC-based method, the TDC-based method and the proposed method, respectively. The 3D tensor data with 80% random missing slices, i.e., SSR = 80%. From left to right, the 3D result and its 3D views on cross-track-azimuth slice, cross-track-height slice and azimuth-height slice are displayed, respectively. Comparing Fig. 6 with referenced Fig. 5, it can be observed evidently that although the scatter points can be resolvable using the conventional 3D RD method with sparse data, higher side-lobes is obvious along the cross-track direction because of the

inadequate sampling. As shown in the second and third lines, HaLRTC and TDC fail to reconstruct the lost elements, which lead to the invalid suppression of side-lobes in 3D imaging result. By contrast, the proposed method can effectively suppress the side-lobes and can get similar 3D imaging performance with 100% data in Fig. 5. Similar to the results from Fig. 4, the imaging performance along the azimuth and height direction changes between different methods are not obvious because the remaining samples on the azimuth-height slices are full sample.

5.3 Performance with different SSRs and SNRs

Different SSRs and SNRs would bring the changes in the imaging performance. To quantitatively evaluate these changes, we compute the mean squared error between the 3D image reconstructed with sparse data $\mathcal{T}_{\text{sparse}}$ and the full-sampled data $\mathcal{T}_{\text{full}}$.

$$\text{MSE} = \frac{\left\|\mathcal{T}_{\text{sparse}} - \mathcal{T}_{\text{full}}\right\|_F}{\|\mathcal{T}_{\text{full}}\|_F} \tag{21}$$

Apparently, we prefer a smaller MSE value, which illustrates the reconstructed signal is much closer to the original signal.

We set up multiple sets of experiments with different SSRs from 10 to 90% under Monte Carlo simulation. The SNR is chosen to be 10 dB. The Monte-Carlo trials is set as 50 to evaluate average MSE. Figure 7 compares average MSEs between four different methods based on sparse data with varying SSRs. It can be expected clearly that the average MSEs of the 3D RD method, the HaLRTC-based method and the TDC-based method overlap totally because the HaLRTC-based and the TDC-based methods are invalid completely. When the SSR is improved, the overall trend for average MSE of all methods is declining, which means the reconstruction accuracy becomes higher. Among these curves, when the SSR is more than nearly 30%, the error is extremely tiny (almost less than 0.1) for the proposed method, whereas the average MSE increases drastically when the SSR is less than 30%. It demonstrates that, if SSR is not excessively low (e.g., 30%), the proposed method gains a reliable imaging performance.

The SNRs are examined ranging from -20 to 20 dB under Monte Carlo simulation. The number of Monte Carlo trials is 50. Figure 8 draws the trend of average MSE on

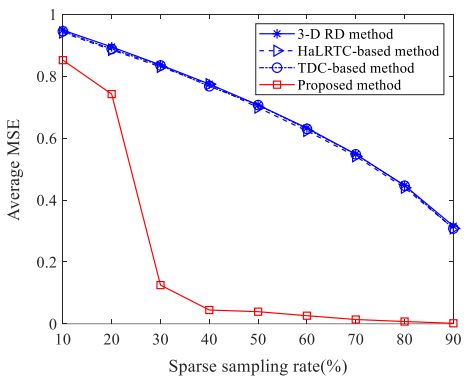

Fig. 7 Trend of average MSE between different methods based on sparse data with various SSRs. The SNR is set to be 10 dB

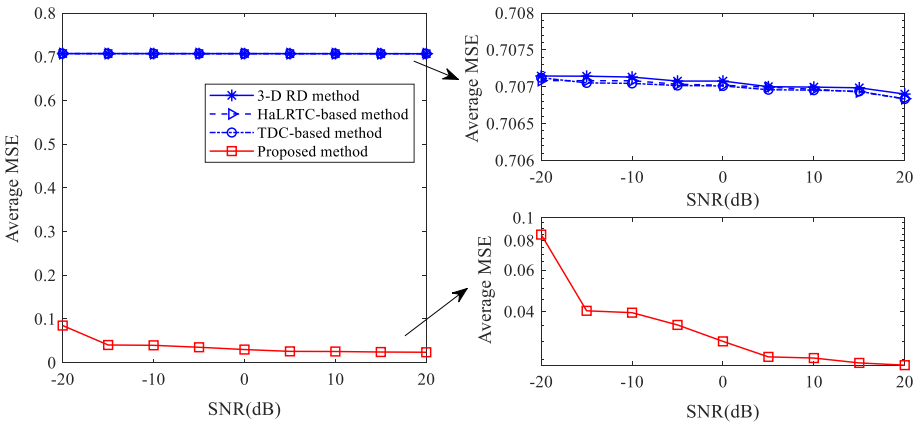

Fig. 8 Trend of average MSE between different methods with various SNRs. The SSR is set as 50%

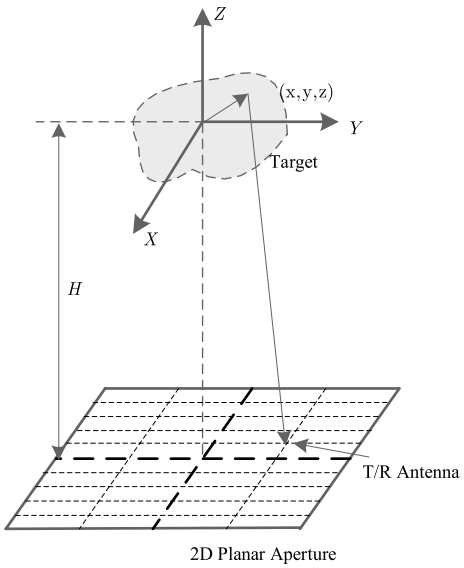

Fig. 9 Experimental principle of real data acquisition

each SNR levels. Although we found that the fluctuation of the curves with 3D RD method, HaLRTC-based method and TDC-based method are not prominent, the average MSEs are slightly reduced with the increasing of SNR, as shown in the top right corner of Fig. 8. Moreover, with the increased SNR, the MSE goes down remarkably. When the SNR reaches − 20 dB, the value of average MSE for the proposed method is still less than 0.1, which implies that the imaging performance can be satisfied with a relatively low SNR. Even so, we can observe from the detail view in the lower right corner that there appears a transition point at the curve of − 15 dB, which indicates when the SNR is very low (less than − 15 dB), the increment of error becomes larger.

5.4 Verification of the proposed algorithm using real dataset

The validation and evaluation of imaging performance for the proposed algorithm are carried out on the real dataset. The experimental principle of real data acquisition is

(a) Signal transmitter (b) Antenna track (c) Foamy plate (d) Eight targets covered with tinfoil

Fig. 10 3D sparse array SAR system

Table 5 Experiment parameters on real data

Parameter	Value
Transmitted frequency	8–12 GHz
Full sweep bandwidth	4 GHz
Frequency step	1 MHz
Center height	2.2 m
Number of azimuth samples	161
Number of cross-track samples	50
Space of azimuth samples	0.01 m
Space of cross-track samples	0.02 m

shown in Fig. 9. A pair of antennas moving along the 2-D track can transmit or receive signal, which can synthesize a virtual 2-D array. Figure 10 displays the signal transmitter, antenna track, foamy plate and eight targets covered with tinfoil. The experiment parameters on real data are shown in Table 5.

In the experiment, the size of the tensor is (50, 161, 1601). The proposed method is applied with $\boldsymbol{\xi} = (32, 1, 1)$. The rank parameters are configured as $\mathbf{L}_1 = [1\ 2\ 4\ 8\ 16\ 32]$, $\mathbf{L}_2 = [1\ 2\ 4\ 8\ 16]$, $\mathbf{L}_3 = [1\ 2\ 4\ 8\ 16\ 32\ 64\ 96\ 128\ 160]$, and $\mathbf{L}_4 = [1\ 2\ 4\ 8\ 16\ 32\ 64\ 128\ 256\ 512\ 1024]$. Figure 11 demonstrates the 3D images reconstructed by various methods based on sparse data with missing slices. Similar to the above conclusions, the targets cannot be satisfactorily reconstructed by ordinary low-rank model. However, the proposed method gets very clear results even though its accuracy is not high. At the same time, the comparison results by four methods with different SSRs are also shown in Fig. 11. With the decrease number of samples, all of the methods obtain more blurred images. When the SSR reaches 20%, the targets cannot distinguish at all by 3D RD and HaLRTC-based method and TDC-based method produced similar results. By contrast, the proposed method obtains significant improvements compared with the other methods. Table 6 shows the average MSE results with three different SSRs. It is demonstrated that the proposed method performs better than the other methods and it was also very robust in terms of the SSR.

6 Conclusion

In this manuscript, we have provided a new idea to realize the 3D imaging of targets for 3D sparse array SAR in embedded space. On the basis of the sparsity and low-rank, the unsampled elements are reconstructed in the multiway delay embedded space by utilizing the tucker decomposition. After tensor complementation, the satisfactory 3D images can be easily achieved by any conventional algorithm. In comparison with other matched filter-based methods, the proposed algorithm has the advantage of acquiring target images

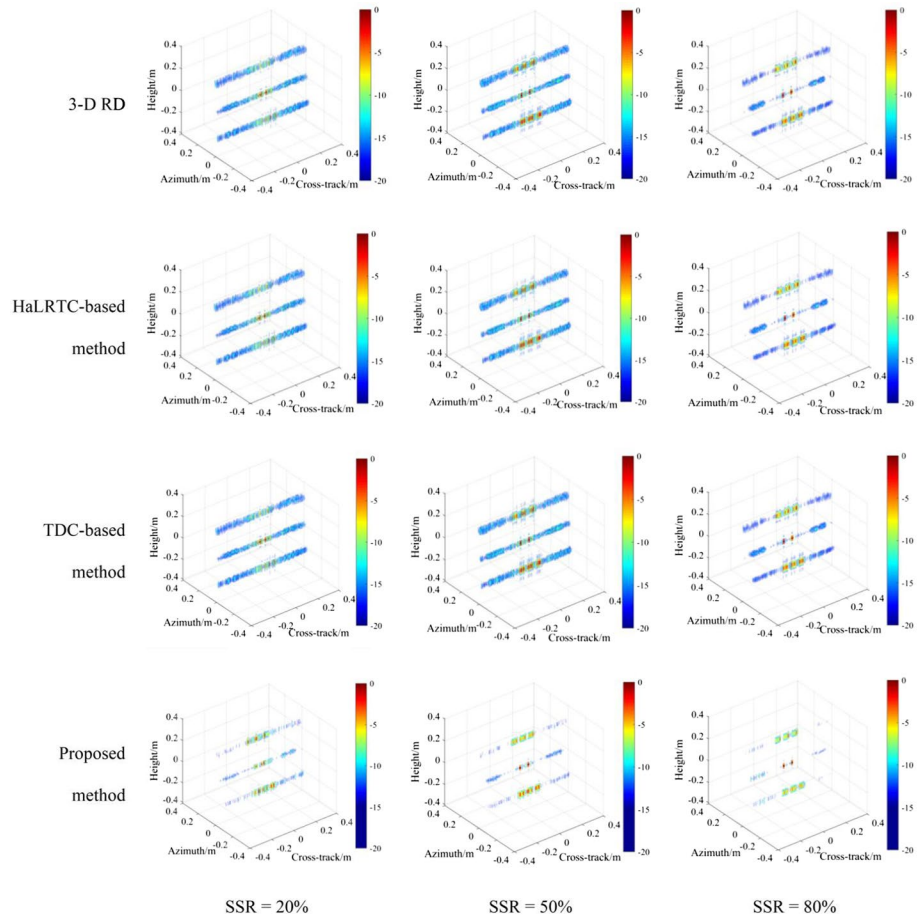

Fig. 11 Comparison of 3D imaging results by sparse data completed with various methods

Table 6 Average MSE results with three different SSRs

Method	Average MSE		
	SSR = 20%	**SSR = 50%**	**SSR = 80%**
3D RD	0.9215	0.7096	0.4458
HaLRTC-based method	0.9215	0.7096	0.4458
TDC-based method	0.9215	0.7096	0.4458
Proposed method	**0.4648**	**0.2558**	**0.1191**

The optimal values are shown in bold

with high-resolution and low side-lobes. Through extensive simulations and experiments on real datasets, the results clearly show that the proposed algorithm can significantly curb the adverse effects resulting from sparse data. In contrast to 3D RD and state-of-the-art tensor completion algorithms, the proposed algorithm can reach similar imaging performance with complete data. Experimental results at different SSR and SNR values also illustrate that the proposed method is robust in the field of SSRs and SNRs. Note that the theoretical derivation of signal model in this paper is based on the first-order Taylor expansion approximation. It is only suitable for the research of point targets in 3D scenes. In the future, 3D imaging will be further deeply studied for area targets with the distributed characteristics.

Abbreviations

3D	Three-dimensional
ALS	Alternating least squares
CS	Compressive sensing
CSAR	Circular SAR
DLLA	Downward-looking linear array
DLSLA	Downward looking sparse linear array
FFT	Fast Fourier transform
HaLRTC	High accuracy low rank tensor completion
InSAR	Interferometric SAR
ISLR	Integrated sidelobe ratio
LASAR	Linear array SAR
MDT	Multiway delay embedding transform
MIMO	Multiple input multiple output
MSE	Mean square error
PSLR	Peak sidelobe ratio
RD	Range Doppler
SAR	Synthetic aperture radar
SNR	Signal noise ratio
SSR	Sparse sampling rate
TC	Tensor completion
TDC	Tucker decomposition

Acknowledgements
The authors thank the corresponding editors and reviewers for providing valuable comments and suggestions for this article.

Author contributions
SZ designed the work, developed the approach, analyzed and interpreted the data, and drafted the manuscript; DD and LZ contributed to literature investigation; CZ contributed to revise the manuscript. The final draft passed the review and confirmation of all authors. All authors read and approved the final manuscript.

Funding
This work was supported by the National Natural Science Foundation of China under Grant 61701508 and Hunan Provincial Natural Science Foundation of China under Grant 2018JJ3613.

Availability of data and materials
Please contact author for data requests.

Declarations

Competing interests
The authors declare that they have no competing interests.

Ethical approval and consent to participate
Not applicable.

Consent for Publication
Not applicable.

Received: 18 March 2022 Accepted: 6 July 2022
Published online: 23 July 2022

References

1. A. Budillon, A. Evangelista, G. Schirinzi, Three-dimensional SAR focusing from multipass signals using compressive sampling. IEEE Trans. Geosci. Remote Sens. **49**(1), 488–499 (2011)
2. D. Massonnet, T. Rabaute, Radar interferometry: limits and potential. IEEE Trans. Geosci. Remote Sens. **31**(2), 455–464 (1993)
3. X. Zhu, R. Bamler, Demonstration of super-resolution for tomographic SAR imaging in urban environment. IEEE Trans. Geosci. Remote Sens. **50**(8), 3150–3157 (2012)
4. O. Ponce, P. Prats-Iraola, M. Pinheiro, M. Rodriguez-Cassola, A. Moreira, Fully-polarimetric high-resolution 3-D imaging with circular SAR at L-Band. IEEE Trans. Geosci. Remote Sens. **52**(6), 1–17 (2013)
5. O. Ponce, P. Prats, M. Rodriguez-Cassola, R. Scheiber, A. Reigber, Processing of circular SAR trajectories with fast factorized back-projection, in *Proceedings of the 2011 IEEE International Geoscience and Remote sensing Symposium, Vancouver, BC, Canada* (2011)
6. H. Wen, Progress in circular SAR imaging technique. J. Radars **1**(2), 124–135 (2012)
7. Q. Bao, Q. Peng, Z. Wang, Y. Lin, W. Hong, DLSLA 3-D SAR imaging based on reweighted gridless sparse recovery method. IEEE Geosci. Remote Sens. Lett. **13**(6), 841–845 (2017)

8. S. Zhang, G. Dong, G. Kuang, Matrix completion for downward-looking 3-D SAR imaging with a random sparse linear array. IEEE Trans. Geosci. Remote Sens. **56**(4), 1994–2006 (2017)
9. T. Gu, G. Liao, Y. Li, Y. Liu, Y. Guo, Airborne downward-looking sparse linear array 3-D SAR imaging via 2-D adaptive iterative reweighted atomic norm minimization. IEEE Trans. Geosci. Remote Sens. **60**(99), 1–13 (2021)
10. Y. Liao, M. Xing, L. Zhang, Z. Bao, A novel modified Omega-K algorithm for circular trajectory scanning SAR imaging using series reversion. EURASIP J. Adv. Signal Process. **2013**(1), 1–12 (2013)
11. C. Gierull, On a concept for an airborne downward-looking imaging radar. AEU-Int. J. Electron. Commun. **53**(6), 295–304 (1999)
12. S. Zhang, M. Yu, G. Kuang, Tensor RPCA for downward-looking 3-D SAR imaging with sparse linear array, in *Proceedings of 15th IEEE International Conference on Signal Processing (ICSP), Beijing, China* (2020)
13. M. Wei, J. Ender, A 3D imaging radar for small unmanned airplanes—ARTINO, in *Proceedings of European Radar Conference, Paris, France* (2005)
14. J. Nouvel, H. Jeuland, G. Bonin, S. Roques, O. Du, J. Peyret, A Ka band imaging radar: DRIVE on board ONERA motorglider, in *Proceedings of 2006 IEEE International Conference on Geoscience Remote Sensing Symposium, Denver, CO, USA* (2006)
15. X. Ren, J. Yang, L. Chen, 3D imaging algorithm for down-looking MIMO array SAR based on bayesian compressive sensing. Int. J. Antennas Propag. **2014**, 1–9 (2014)
16. S. Zhang, G. Dong, G. Kuang, Superresolution downward-looking linear array three-dimensional SAR imaging based on two-dimensional compressive sensing. IEEE J. Sel. Top. Appl. Earth Obs. Remote Sensing **9**(6), 2184–2196 (2016)
17. Q. Wei, M. Martorella, J. Zhou, H. Zhao, F. Qiang, Three-dimensional inverse synthetic aperture radar imaging based on compressive sensing. IET Radar Sonar Navig. **9**(4), 411–420 (2015)
18. J. Liu, P. Musialski, P. Wonka, J. Ye, Tensor completion for estimating missing values in visual data. IEEE Trans. Pattern Anal. Mach. Intell. **35**(1), 208–220 (2013)
19. Y. Zheng, T. Huang, T. Ji, X. Zhao, T. Jiang, T. Ma, Low-rank tensor completion via smooth matrix factorization. Appl. Math. Model. **70**, 677–695 (2019)
20. T. Kolda, Tensor decompositions and applications. SIAM Rev. **51**(3), 455–500 (2009)
21. J. Yan, W. Pu, S. Zhou, H. Liu, Z. Bao, Collaborative detection and power allocation framework for target tracking in multiple radar system. Inf. Fusion **55**, 173–183 (2020)
22. J. Yan, J. Dai, W. Pu, H.S. Liu, M. Greco, Target capacity based resource optimization for multiple target tracking in radar network. IEEE Trans. Signal Process. **69**(99), 2410–2421 (2021)
23. W. He, N. Yokoya, L. Yuan, Q. Zhao, Remote sensing image reconstruction using tensor ring completion and total variation. IEEE Trans. Geosi. Remote Sens. **57**(99), 8998–9009 (2019)
24. J. Zhang, M. Qin, C. Bai, J. Zheng, Missing elements recovery using low-rank tensor completion and total variation minimization, in *Proceedings of IFTC 2019: Digital TV and Wireless Multimedia Communication* (Springer, Singapore, 2019), pp. 35–48
25. W. Qiu, J. Zhou, Q. Fu, Tensor representation for three-dimensional radar target imaging with sparsely sampled data. IEEE Trans. Comput. Imaging **6**, 263–275 (2019)
26. W. Feng, J. Friedt, G. Nico, 3-D ground-based imaging radar based on C-band cross-MIMO array and tensor compressive sensing. IEEE Geosci. Remote Sens. Lett. **16**(10), 1585–1589 (2019)
27. F. Sedighin, A. Cichocki, T. Yokota, Q. Shi, Matrix and tensor completion in multiway delay embedded space using tensor train, with application to signal reconstruction. IEEE Signal Process. Lett. **27**(99), 810–814 (2020)
28. T. Yokota, Missing slice recovery for tensors using a low-rank model in embedded space, in *Proceedings of 2018 IEEE Conference on Computer Vision and Pattern Recognition. Lake City, UT, USA* (2018)
29. J. Dai, Y.Q. Jin, Scattering simulation and reconstruction of a 3-D complex target using downward-looking step-frequency radar. IEEE Trans. Geosci. Remote Sens. **49**(10), 4035–4047 (2011)
30. Y. Li, K. Liu, J. Razavilar, A parameter estimation scheme for damped sinusoidal signals based on low-rank Hankel approximation. IEEE Trans. Signal Process. **45**(2), 481–486 (1997)
31. M. Filipovi, A. Juki, Tucker factorization with missing data with application to low-n-rank tensor completion. Multidimens. Syst. Signal Process. **26**, 677–692 (2015)
32. J. Wang, G. Zhao, D. Wang, G. Li, Tensor completion using low-rank tensor train decomposition by Riemannian optimization, in *Proceedings of 2019 Chinese Automation Congress (CAC), Hangzhou, China* (2019)
33. S. Zhang, Y. Zhu, G. Kuang, Imaging of downward-looking linear array three-dimensional SAR Based on FFT-MUSIC. IEEE Geosci. Remote Sens. Lett. **12**(4), 885–889 (2015)
34. L. Du, Y. Wang, W. Hong et al., A three-dimensional range migration algorithm for downward-looking 3D-SAR with single-transmitting and multiple-receiving linear array antennas. EURASIP J. Adv. Signal Process. **2010**(11), 1–12 (2010)

Publisher's Note